Controlling a quantum point junction on the surface of an antiferromagnetic topological insulator

Nicodemos Varnava,[1,*] Justin H. Wilson,[1] J. H. Pixley,[1] and David Vanderbilt[1]

[1] *Department of Physics & Astronomy, Center for Materials Theory, Rutgers University, Piscataway, New Jersey 08854, USA*

The abstract notion of topology has led to profound insights into real materials. Notably, the surface and edges of topological materials can host physics, such as unidirectional charge or spin transport, that is unavailable in isolated one- and two-dimensional systems. However, to fully control the mixing and interference of edge-state wave functions, one needs robust and tunable junctions. We propose to achieve this control using an antiferromagnetic topological insulator that supports two distinct types of gapless unidirectional channels on its surface, one from antiferromagnetic domain walls and the other from single-height steps. The distinct geometric nature of these edge modes allows them to intersect robustly to form quantum point junctions, and their presence at the surface makes them subject to control by magnetic and electrostatic tips like those used in scanning probe microscopes. Prospects for realizing such junctions are encouraged by recent material candidate proposals, potentially leading to exciting applications in quantum computing and sensing.

I. INTRODUCTION

Surface and edge-state engineering of topological materials offers great promise for future electronic devices. Owing to the topological properties of the bulk of the material, surface states emerge that are protected from elastic and inelastic scattering. In particular, the community realized early on that topologically-protected chiral (one-way) or helical (two-way) edge states provide dissipationless "quantum wires"[1,2] with potential applications in sensor, low-power computing, and quantum information technologies. A crucial part of engineering such wires requires robust and tunable junctions between edge states.

Strikingly, chiral edge states provide directional control of carrier propagation and (topological) protection against impurity backscattering. This was first demonstrated for quantum Hall edge states in 2D electron gases, but these systems require very low temperature and external magnetic fields. A potentially more practical approach to engineering chiral edge states is at the boundary of a 2D quantum anomalous Hall or "Chern" insulator.[3] Experimentally this was first realized in thin films of magnetically doped topological insulators (TI).[4] Unfortunately the inhomogeneity of the magnetic dopants leads to inevitable disorder[5] and as a result the quantized response is observed at much lower temperatures than the magnetic gap and Curie temperature allow; to date the state of the art is around $\sim 1K$.[6–9] More recently, the discovery of the quantum anomalous Hall effect in twisted bilayer graphene[10,11] and 5-layer $MnBi_2Te_4$[12] holds promise for the realization of topologically protected chiral channels at higher temperatures, due in part to the absence of magnetic-impurity disorder.[13]

In its bulk version, $MnBi_2Te_4$ belongs to a class of 3D materials that have been variously described as intrinsic magnetic topological insulators,[12,14–16] axion insulators[17–19] and second-order topological insulators.[20–22] The essential idea is to identify a material whose magnetic symmetry group enforces[19] a quantized bulk axion coupling[23,24] of $\theta = \pi$, as in an ordinary 3D TI, but does not enforce the presence of gapless surface states. Instead, gapped surfaces can appear naturally on such materials. When they do, they exhibit a half-quantized surface anomalous Hall conductivity, i.e., an odd integer times $e^2/2h$, whose sign is determined by details of the magnetic order at the terminating surface. Thus, manipulation of the surface termination and/or magnetic order in one region of the surface relative to a neighboring patch, or on one facet relative to another that meets it at a "hinge," can give rise to a chiral edge channel at the boundary between these patches or facets.[18]

In this work we develop a theoretical description for the creation and manipulation of chiral edge channels on the surface of an antiferromagnetic (AFM) TI. This class of materials was introduced theoretically by Mong and Moore[25] and has recently become the focus of intense research with various candidates such as $MnBi_2Te_4$[26], $MnBi_4Te_7$[27], $EuIn_2As_2$[28] and NpBi[29] appearing in the literature. Motivated by these recent developments and the fact that there is in principle no reason why both the bulk and surface gaps could not be on the order of hundreds of meV, allowing for potential room-temperature device operation, we propose and explore the properties of a novel *quantum point junction* (QPJ) at the surface of an AFM TI.

Figure 1**a**, **b** shows a prototypical spin arrangement in an AFM TI. The magnetic ordering is A-type AFM, i.e., with magnetization uniform in-plane but alternating from plane to plane along the stacking direction, which we take to be along $\hat{\mathbf{z}}$. As described in Ref. 25, each individual layer can be thought of as adiabatically connected to a 2D Chern insulator, with the sign of the Chern number alternating from layer to layer. The sign of the surface anomalous Hall conductivity of $\pm e^2/2h$ is thus determined by the magnetic orientation of the last

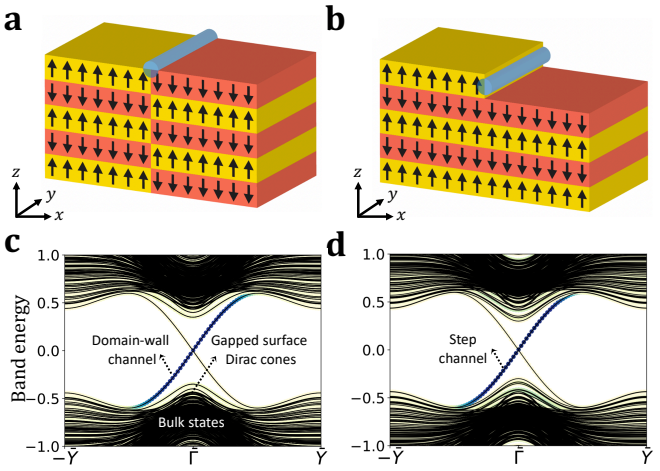

FIG. 1. **a**, **b**, Depiction of the chiral channel (blue cylinder) at the surface of an A-type AFM TI due to **a**, a bulk domain wall **b**, a surface step. **c**, **d**, Surface band structures along (001) in the presence of **c**, a bulk domain wall **d**, a surface step. The projection of the states on the chiral channels (blue cylinder) in **a**, **b**, are also shown (blue markers) to illustrate the localization of the massless Dirac fermions that disperse linearly along the channel direction at low energy with velocities **c**, $v_{\rm dw}$ and **d**, $v_{\rm st}$. The description of the model Hamiltonian can be found in Methods. Energies are expressed in terms of the onsite energy m in Eq. (8).

layer at the surface. As a result, two kinds of 1D chiral channels can occur at the surface. As shown in Fig. 1**a**, the emergence of a bulk AFM domain wall at the surface reverses the sign of the anomalous Hall conductivity on either side of the resulting line defect, which therefore carries a topologically protected chiral channel we refer to as a *domain-wall channel*. Alternatively, even if no bulk AFM domain walls are present, a single-height step can occur on the surface, as shown in Fig. 1**b**. If it does, it also marks a sign reversal of the anomalous Hall conductivity when crossing the step, and thus carries a chiral edge channel as well. We will refer to this as a *step channel*.

Figure 1**c**, **d**, shows the manifestation of the domain-wall and step channel in the surface band structure as described in the context of a tight-binding model used throughout this work (see Methods). The presence of either of these defects results in 1D linear dispersions in the otherwise gapped bulk and surface spectrum of the AFM TI. The states that comprise the chiral bands are exponentially localized in the vicinity of the channel, and host 1D massless Dirac fermions.

The novel opportunity opened by the presence of two different kinds of 1D chiral channels at the surface, is that these can be made to intersect, as shown in Fig. 2**a**, and such intersections are expected to remain thermodynamically stable. In contrast, as illustrated in Fig. 2**b**, an intersection between two surface steps can easily evolve via a pinch-off event into a configuration in which an isthmus of constant surface height separates the steps; indeed, the width of such an isthmus will tend to grow due to the line tensions of the steps, and the quantum junction will have been removed. A similar mechanism affects the intersection of two domain walls. Instead, an intersection of a domain wall and step cannot easily be removed, providing an opportunity for engineering a robust QPJ. In fact, these junctions can appear naturally and were recently seen at the surface of the putative AFM TI $MnBi_2Te_4$.[30] Moreover, the fact that this junction occurs at an exposed surface, not at a buried interface, opens opportunities for its manipulation by scanning tips of the kind used in scanning tunneling microscopy (STM) and related methods. Here we are interested in local probes that affect magnetic moments and the electric potential and will refer to them as magnetic and electrostatic STM tips respectively.

In what follows we explore the properties of the QPJ by constructing a tight-binding Hamiltonian associated with the system depicted in Fig. 2**a** and performing dynamic wave-packet (WP) simulations. Importantly, the creation and detection of single-electron WPs on quantum Hall edge channels has been demonstrated experimentally.[31] In fact it has been shown[32–34] that using modulated bias voltage one can create a minimal excitation known as a Leviton,[35–37] where the Fermi sea re-organizes itself and a single electron (with no accompanying hole) is emitted in the conduction band. While these techniques directly apply to our proposal, a major benefit of our approach is the formation of thermodynamically stable point junctions which would be difficult to accomplish using quantum Hall edges. In fact, setups like those depicted in the inset of Fig. 2**b**, where two chiral channels come in close proximity enabling tunnelling between them, have long been studied in 2D electron gases[38,39] and are known as *quantum point contacts* (QPC), a terminology that we have adopted for the junctions proposed here.

As we show below the scattering of WPs at the proposed QPJ can be described by a two level quantum system. In this description the state of the WP is represented by a qubit whose entries correspond to the amplitude (magnitude and phase) of the WP on the two incoming or outgoing channels. Furthermore, the QPJ acts as a unitary quantum gate, or an S-matrix that characterizes the scattering. Remarkably, we find that magnetic and electrostatic STM tips in proximity with the junction can be used to realize any single-qubit gate. In addition, we show that the effect of symmetry breaking terms and weak disorder can be "gauged away using the two tips. Finally we take a look at potential applications of the QPJ in quantum computing and sensing.

II. EXTRACTING THE S MATRIX

We begin by considering the WP dynamics at the surface of an AFM TI. Figure 3**a** shows the calculated time evolution of a WP on a single domain-wall chan-

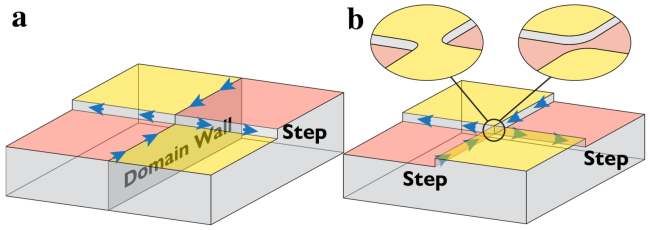

FIG. 2. **a**, The intersection of a domain-wall channel with a step channel results in a thermodynamically stable junction, i.e., small surface deformations can only move the junction but not remove it. **b**, The intersection of two step channels (or two domain-wall channels) is unstable. The inset shows how small deformations remove the junction. Blue arrows indicate the direction of propagation on the chiral channels, while orange and yellow surfaces indicate whether the anomalous Hall conductivity is $\pm e^2/2h$ respectively.

nel, while Fig. 3**b**, that of a WP in the presence of the QPJ in Fig. 2**a** (see also Supplemental Information for time-evolution animations). In both cases the dissipationless channels are protected from back-scattering by the insulating bulk and surface gaps. The wave function of the WP is thus exponentially confined to the vicinity of the one-dimensional channel, and it travels with a constant group velocity along the channel. In Fig. 3**b**, a WP enters along the domain-wall channel, gets split by the QPJ, and then the two components travel away from the QPJ along the step channels. Later we shall consider configurations in which multiple consecutive scattering events occur.

To understand the behaviors observed above, we note that the wave function of a WP propagating along a single domain-wall channel in direction y, as in Fig. 3**a**, can be well approximated[40] as

$$\Psi^{\rm dw}_{\sigma\tau}(x,y,z,t) = \chi^{\rm dw}_{\sigma\tau}(x,z) f(y - y_0 - v_{\rm dw} t)\,. \qquad (1)$$

Here $\chi^{\rm dw}_{\sigma\tau}(x,z)$ captures the transverse shape (x,z) and spin-orbital character (σ,τ indices respectively) of the WP[40], while $f(y)$ is the envelope function of the WP, which we take to be a Gaussian. The WP is launched from position y_0 at time $t=0$ and travels with group velocity $v_{\rm dw}$ (which is set by the surface state dispersion in Fig. 1**c**). In modeling at this level we neglect spreading of the WP, which we find to be negligible in our simulations. Similar considerations apply to the propagation of a WP on a step along x traveling with group velocity $v_{\rm st}$ (that is set by the surface state dispersion in Fig. 1**d**).

We now consider the scattering event depicted in Fig. 3**b**, where an incoming WP splits after encountering the QPJ. We will use unprimed labels a and b to refer to the two incoming domain-wall channels of Junction 1, as in Fig. 3**c**. Note that the extra junctions are the result of in-plane periodic boundary conditions. The incoming initial conditions are specified by amplitudes $\phi_a = 1$ and $\phi_b = 0$. Now let t_1 indicate a time after the scattering through Junction 1 is complete, but before Junction 2 is encountered. We label the two outgoing step channels as a' and b', adopting once and for all the arbitrary convention that $a \to a'$ and $b \to b'$ result from taking left turns, as shown in Fig. 3**c**. As illustrated in Fig. 3**b**, one component of the WP moves to the right and the other to the left, with velocities $v_{\rm st}$ and $-v_{\rm st}$ respectively. At time t_1 both will be centered at a distance x_1 relative to the junction, so in general we expect to find

$$\begin{aligned}\Psi^{\rm st}_{\sigma\tau}(x,y,z,t_1) = {}& \phi_{a'}\tilde{\chi}^{\rm st}_{\sigma\tau}(y,z) f(x+x_1) \\ & + \phi_{b'}\chi^{\rm st}_{\sigma\tau}(y,z) f(x-x_1)\,. \end{aligned} \qquad (2)$$

Here $\phi_{a'}$ and $\phi_{b'}$ are the amplitudes (magnitude and phase) describing scattering from incoming channel a into channels a' and b' respectively, and $\tilde{\chi}^{\rm st}$ is the time-reversed partner of $\chi^{\rm st}$. These expectations are well reproduced in our full numerical calculations which therefore allow us to extract the amplitudes $\phi_{a'}$ and $\phi_{b'}$.

Similar calculations, where the incident WP approaches Junction 1 along the $-\hat{y}$ direction on channel b, allow us to extract the corresponding amplitudes that result for initial conditions of $\phi_a = 0$ and ϕ_b=1. Thus, we can model a combined scattering event via

$$\begin{pmatrix}\phi_{a'}\\ \phi_{b'}\end{pmatrix} = S \begin{pmatrix}\phi_a \\ \phi_b\end{pmatrix} \qquad (3)$$

where the elements of the S-matrix are determined by the four complex amplitudes discussed above.

In this way, the evolution of the system of propagating WPs is mapped onto that of a two-level quantum system, so that it is enough to restrict S to be an SU(2) matrix.[41] The characterization of a junction by such an S-matrix is a central element of our theory. It is illustrative to represent the initial or final state as a point on the Bloch sphere,

$$\begin{pmatrix}\phi_a\\ \phi_b\end{pmatrix} = \begin{pmatrix}\cos(\theta/2)\\ e^{i\phi}\sin(\theta/2)\end{pmatrix}, \qquad (4)$$

where θ determines the relative WP magnitude on channels a and b and ϕ their phase difference, as illustrated in Fig. 3**d**.

Each junction scattering event can then be described by the action of the corresponding junction S-matrix on the spinor representation of the channel states, regarded as a *qubit state*, and the result of consecutive QPJ scattering events, as in Fig. 3**e**, corresponds to the action of consecutive *gates* acting on these qubits as illustrated in Fig. 3**f**.

Let us now return to a more specific discussion of our full time-evolution calculations, and our analysis of them in terms of the framework sketched above. Figure 3**e**, shows the time evolution of a WP initiated on channel a. The WP propagates towards and then scatters at Junction 1, splitting into two equal parts. Later the two WPs pass through Junction 2, interfering destructively and constructively on outgoing channels a' and b' respectively. As promised, we can describe the time evolution

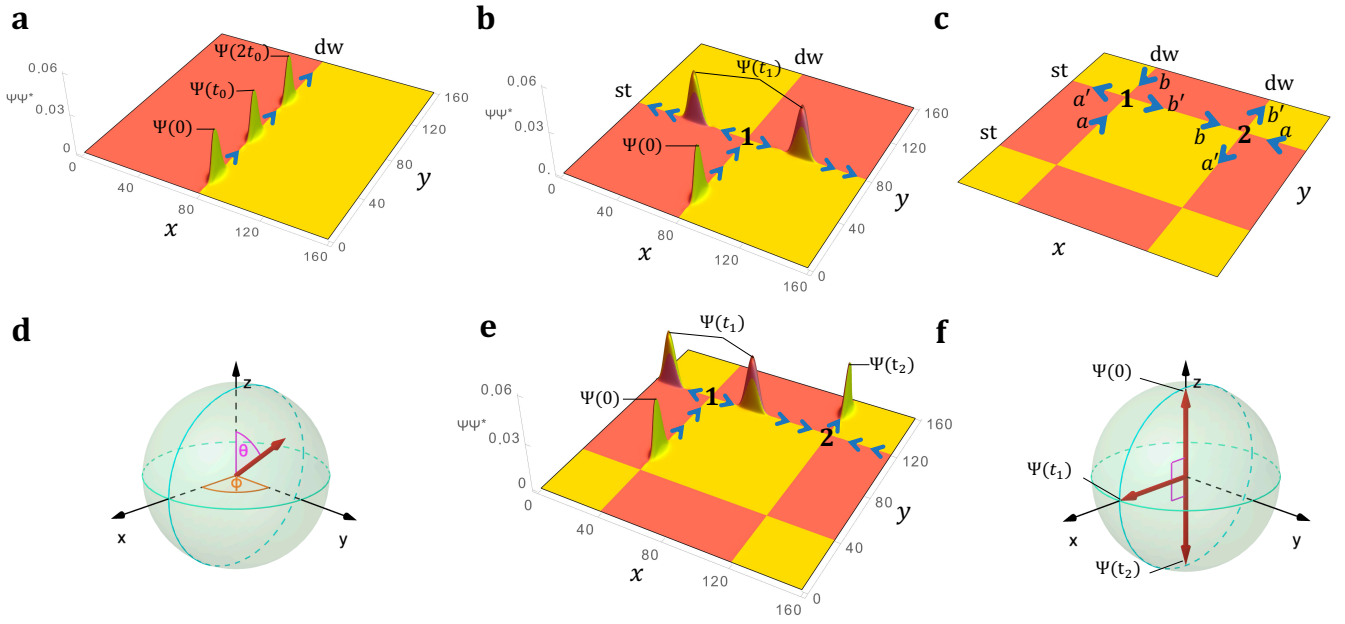

FIG. 3. **a**, Snapshots of the WP showing the propagation on the domain-wall channel. **b**, A WP scatters at Junction 1 and splits into two spatially separated outgoing components of the wavefunction. **c**, Channel labeling convention for Junction 1 and 2. **d**, Qubit representation of a WP state on the Bloch sphere. **e**, The initial WP splits after encountering Junction 1, the two components then meet at Junction 2, interfering destructively on channel a' and constructively on channel b'. **f**, Qubit representation of the time evolution in **e**. WP plots in **a**, **b**, **e**, are calculated from the (001)-projected probability densities at different times. Time-evolution animations showing the WP dynamics in **a**, **e** are provided in the Supplemental Information.

of the WP configuration as a qubit passing through two gates. Indeed, using the convention of Fig. 3**c**, the calculated S matrix of Junction 1 and 2 corresponds to the Hadamard gate

$$S_1 = S_2 = \frac{1}{\sqrt{2}}\begin{pmatrix} 1 & -1 \\ 1 & 1 \end{pmatrix}, \tag{5}$$

so that the final state is related to the initial one by applying the Hadamard gate twice. Geometrically the S matrix expressed as

$$S = R_{\hat{\mathbf{n}}}(\varphi) = e^{-i\frac{\varphi}{2}\hat{\mathbf{n}}\cdot\boldsymbol{\sigma}} \tag{6}$$

describes a qubit rotation by an angle φ through an axis $\hat{\mathbf{n}}$ and $\boldsymbol{\sigma} = (\sigma_x, \sigma_y, \sigma_z)$ is a vector of Pauli matrices. Since $S_1 = S_2 = R_{\hat{\mathbf{y}}}(\pi/2)$, each application rotates the qubit by 90° around the $\hat{\mathbf{y}}$ axis of the Bloch sphere, resulting in an overall reversal of the pseudospin as shown in Fig. 3**f**.

III. CONTROLLING THE S MATRIX

Before explaining how the control of the S matrix is achieved, it is illustrative to break down the action of S into three stages. First we have the propagation along the incoming channels; since these cannot scatter into one another, this is represented by a diagonal matrix $S_{\rm dw}$. Then there is the scattering $S_{\rm pj}$ at the QPJ itself, followed by another channel-diagonal propagation $S_{\rm st}$ on the outgoing step channels. The overall S matrix can then be written in terms of the Pauli matrices as

$$S = S_{\rm st}S_{\rm pj}S_{\rm dw} = e^{-i\gamma\sigma_z/2}e^{-i\beta\sigma_y/2}e^{-i\alpha\sigma_z/2}, \tag{7}$$

where $S_{\rm pj}$ is expressed as a real orthogonal matrix because the phases can be absorbed into $S_{\rm dw}$ and $S_{\rm st}$. Remarkably, (α, β, γ) are exactly the three Euler angles that can be used to express any SU(2) matrix. Thus control over the three Euler angles results in a *universally programmable gate*, which we now demonstrate.

To control the S matrix, we will use two local probes in the vicinity of the junction. The first one, which we refer to as a magnetic STM tip, affects the local magnetic moments, and as we shall see, controls the magnitudes of the S matrix. The second probe is an electrostatic STM tip modifying the site energies under the tip, thus controlling the phases of the S matrix. The effect of the magnetic tip is controlled through the coefficient $V_{\rm Z}$, and that of the electrostatic tip through $V_{\rm G}$, both acting in the local vicinity of the junction. For more details on how this is modeled, see Eq. (9) in Methods.

a. Magnitude control. We set $V_{\rm G} = 0$, leaving the electric potential constant throughout the crystal so that no extra phase evolution occurs during the propagation ($\alpha = \gamma = 0$), and we vary the strength of the magnetic tip $V_{\rm Z}$. This affects the left-right magnitude splitting, i.e., $S = R_{\hat{\mathbf{y}}}(\beta) = e^{-i\beta\sigma_y/2}$ in Eq. (7), with $\beta = \beta(V_{\rm Z})$. To un-

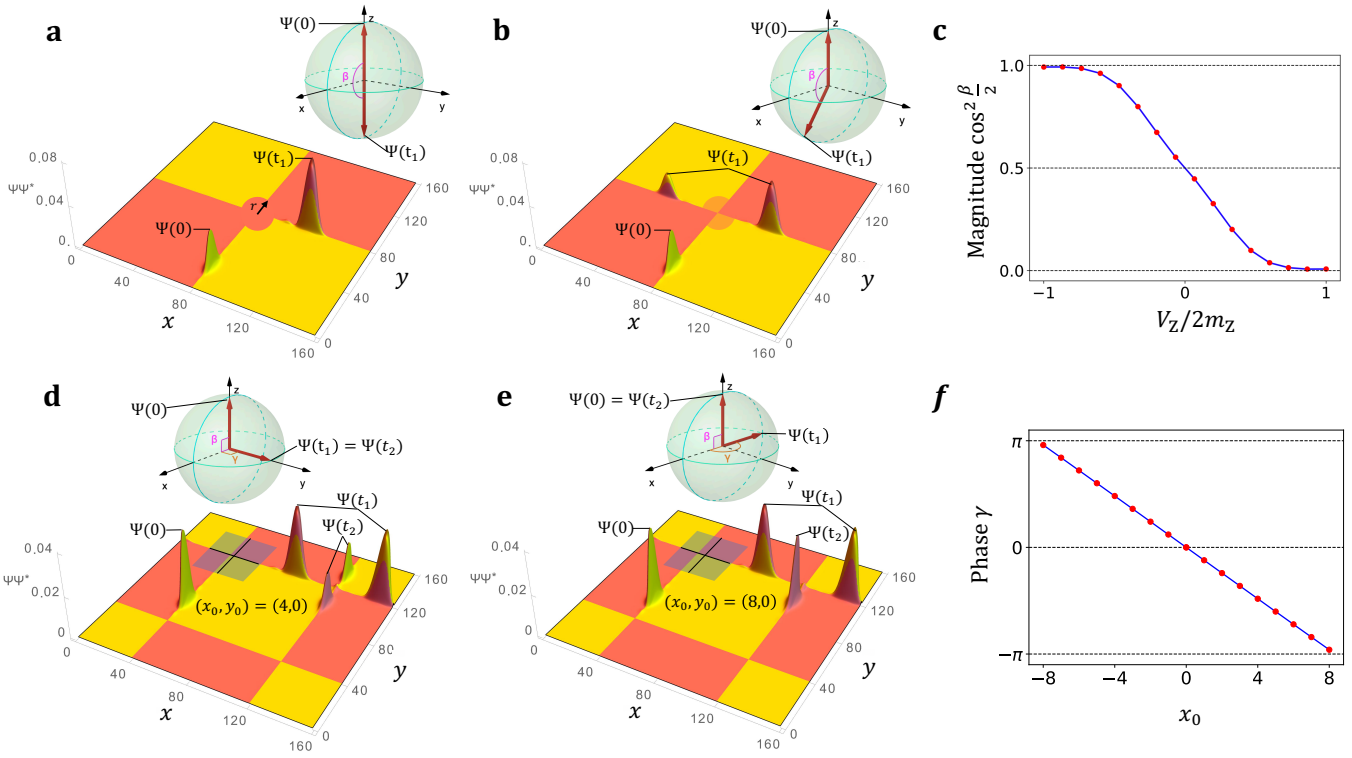

FIG. 4. Magnitude **a**-**c**, and phase **d**-**f**, manipulation of S_1. **a**, The magnetic STM tip with $V_Z = 2m_Z$ in Eq. (9) (see Methods), has polarized the surface spins in a circular region centered at the junction resulting in two uncoupled channels. **b**, Partially polarized region with $V_Z = 0.4m_Z$ causes unequal splitting of the WP. **c**, Numerical calculation of the magnitude splitting $\cos^2\beta/2$ as a function of V_Z. Each value corresponds to the integral of $|\Psi(t_1)|^2$ on channel a' of Junction 1. **d**,**e**, Applying the electrostatic STM tip with $V_G = 0.6$ in Eq. (9), at Junction 1 induces a phase difference between the outgoing WPs which then affects how they interfere at Junction 2. **d**, The center of the rectangular region Ω_G is chosen so that $\gamma = \pi/2$. **e**, Same but we set $\gamma = \pi$ making the WPs constructively (destructively) interfere on channel $a(b)$ of Junction 2. **f**, Numerical calculation of the angle γ from the relative phase of the outgoing WPs at t_1 as a function of x_0. The phases of the outgoing WPs are determined from the inner product between $\Psi(t_1)$ in the presence and absence of the phase gate. Time-evolution animations showing the scattering events in **a**, **b**, **d**, **e** are provided in the Supplemental Information.

derstand the mechanism behind the magnitude control, first consider the extreme scenario depicted in Fig. 4**a**. Here a strong magnetic STM tip has polarized the surface magnetization in the vicinity of the junction (orange circular region), forcing the anomalous Hall conductivity to be uniformly $+e^2/2h$ in that area (see Methods). This essentially "removes" the junction, and the WP is completely transferred from the domain-wall (channel a) to the edge of the step (channel b'), so that $S_1 = R_{\hat{\mathbf{y}}}(\pi)$. An example of partial polarization, is shown in Fig. 4**b**, while the results of tuning V_Z over the entire range of tip strength is shown in Fig. 4**c**, where we plot the numerically calculated value of $\cos^2(\beta/2)$, which represents the asymmetry between left- and right-scattered WPs, as a function of V_Z. This demonstrates the universal control of the Euler angle β using a magnetic STM tip.

b. Phase control. To illustrate the phase control, we set $V_Z = 0$, fix V_G to a non-zero value (see Eq. (9) in Methods), and control the position of the electrostatic tip. Then $S_j = R_{\hat{\mathbf{z}}}(\gamma)R_{\hat{\mathbf{y}}}(\pi/2)R_{\hat{\mathbf{z}}}(\alpha)$, where α and γ are determined by the position (x_0, y_0) of the tip relative to the junction, as described by Eq. (10) (see Methods). The electrostatic tip is depicted as a shaded square with origin (x_0, y_0) in Fig. 4**d**,**e**. In fact, our choice of $\phi_a = 1$ and $\phi_b = 0$ simplifies the situation, since $R_{\hat{\mathbf{z}}}(\alpha)$ just corresponds to an overall phase, which is not of interest. Physically, the WP splits equally at the first junction ($\beta = \pi/2$), and the electrostatic STM tip, corresponding to the second term in Eq. (9), is then used to control the relative phases of the outgoing WPs via the $R_{\hat{\mathbf{z}}}(\gamma)$ term.

In Fig. 4**d**-**f**, we illustrate the phase control by applying the electrostatic gate on Junction 1. To see the effects of the phase manipulation, we consider the interference that conveniently occurs when the WPs meet again (due to periodic boundary conditions in x and y) at Junction 2. In Fig. 4**d**, the electrostatic tip is centered four unit cells to the right at $(x_0, y_0) = (4, 0)$, which approximately makes $\gamma = \pi/2$ so that $S_1 = R_{\hat{\mathbf{z}}}(\pi/2)R_{\hat{\mathbf{y}}}(\pi/2)$, while $S_2 = R_{\hat{\mathbf{y}}}(\pi/2)$ as before. After scattering at Junction 1 the outgoing WP, whose state corresponds to a vector pointing along the $+y$ direction of the Bloch sphere, becomes the incoming WP at Junction 2. Since Junction

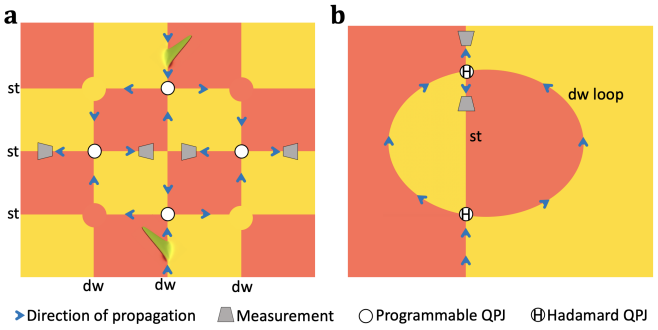

FIG. 5. Schematic of **a**, a four-level quantum system with four programmable gates **b**, a magnetometer consisting of a domain-wall channel loop intersected by a step.

2 acts as a rotation around the y-axis, it does not affect the qubit state of the WP. Similarly, in Fig. 4**e**, we set $(x_0, y_0) = (8, 0)$, so that after encountering Junction 1 the qubit state points along $-\hat{\mathbf{x}}$, and after Junction 2 it returns to its initial $+\hat{\mathbf{z}}$ state. In Fig. 4**f**, we present a numerical calculation of γ versus x_0. This is done by calculating the phase of the WPs just after it scatters off Junction 1. We find a linear behavior as expected from Eq. (10).

In summary, using the two STM tips we can control α, β, and γ independently in Eq. (7), so that the junction can be made to implement any SU(2) gate.

c. Symmetries. Our QPJ has many artificial symmetries that in any real application will be absent. For example, we have seen that it naturally implements the Hadamard gate so that the WP splits equally after encountering the QPJ; this behavior is enforced by the mirror symmetries M_x and M_y of the bulk Hamiltonian, and should not be expected in general. We demonstrate in the Supplemental Information that breaking these symmetries does not affect the ability of our protocol to control the S matrix.

d. Stability to disorder. A significant advantage of the QPJ design presented here is that the chiral channels on the domain walls and steps cannot back-scatter and are therefore expected to be robust against the presence of weak disorder (i.e, such that the average bulk and surface gaps remains open). We demonstrate this topological protection of the QPJ by introducing disorder into our model via a short-ranged random potential that is sampled from a Gaussian distribution. Although the qubit gets dephased in a different way for each realization of disorder, as we demonstrate in the Supplemental Information, the electrostatic tip can be used to recalibrate the QPJ. This allows us to remove the random offsets arising from the specific impurity configuration, thus enabling the control of the junction even in the presence of weak disorder.

IV. APPLICATIONS

Having theoretically characterized the QPJ, we turn now to a discussion of its potential applications in quantum computing and sensing.

a. Quantum computing. Up to this point we have considered systems where an electron WP is injected into the system and after encountering one or more QPJs can be detected at either of two output channels with probabilities given by $|\phi_{a'}|^2, |\phi_{b'}|^2$. More generally one can imagine networks of junctions that implement an N-level quantum system, that is N channels where electrons can be detected. An example of a four-level quantum system is shown in Fig. 5**a**. Here a network of junctions has been constructed by intersecting parallel domain-wall with parallel step channels. Four of the junctions have been polarised so as to guide the WPs while four others can be programmed. While Fig. 5**a** uses four junctions to produce a particular four-by-four unitary, universal control over an SU(4) matrix can be achieved with proper placement of six junctions via Givens rotations.[42] In fact, this can be scaled up to any SU(N) using at most $N(N-1)/2$ of the fully tunable SU(2) gates we have constructed.

We should note that this approach to quantum-computing belongs to a broader class of approaches associated with *flying-qubit quantum computation*.[43,44] To date, the discussion has largely focused on the creation and manipulation of WPs on integer quantum-Hall edge states.[45] Importantly, the techniques developed for that approach are transferable to our proposal. A major advantage of our QPJ approach is that it is quite natural for domain walls and steps to intersect, unlike other approaches where there is no obvious mechanism to produce intersections (as in the case of quantum Hall edges). Furthemore, an AFM TI does not require an external magnetic field to operate, which makes it attractive in microelectronic applications. The time scale of quantum computation is determined by the Fermi velocity of the chiral surface states (denoted $v_{\rm dw}$ and $v_{\rm st}$), which typically is of the order $\hbar v_{\rm F} \sim 1\text{eV}\cdot\text{Å}$. Thus, the application of quantum gates is 10^3 times faster than those of other prominent quantum computation schemes.[46,47] We also remark that the chiral nature of the surface channels composed of 1D massless Dirac fermions can interface with chiral Majorana fermion qubit architectures, e.g., with the digital qubit gate that has been proposed at quantum anomalous Hall insulator and topological superconductor junctions.[48]

b. Quantum Sensor: Beyond quantum computing, a perhaps simpler application of our QPJ is as a sensitive magnetic sensor. Consider a domain-wall loop channel intersected by a step channel as in Fig. 5**b**. In this case we assume a current flowing from the bottom of Fig. 5**b**, through the step channel to scatter at the first Hadamard QPJ where it splits equally into two components. The two components then flow on the two domain-wall channels comprising the loop and meet at the second QPJ. If

no external magnetic flux threads the loop the two currents will recombine just like in Fig. 3**e**, and flow only in the channel that is inside the loop. In contrast, if an external magnetic flux threads the loop the two currents will pick up a relative Aharonov-Bohm phase which affects their interference, resulting in a non-zero current in the channel flowing towards the top of the figure. Thus by measuring the output current one can determine the local magnetic field inside the domain-wall loop region.

V. CONCLUSION

In this work, we have demonstrated the novel opportunity offered by antiferromagnetic topological insulators to realize robust quantum point junctions at their surfaces, owing to the existence of two types of chiral channels (domain-wall and step) appearing on their surfaces. By identifying the two incoming channels with the two "code" states of a qubit, our results show that the S matrix of the quantum point junction acts as a single-qubit gate rotating the state vector of the qubit to produce the two outgoing channels. Furthermore, we have shown that magnetic and electrostatic tips from scanning tunneling microscopy can modify the junction so that its S matrix can perform any rotation on the Bloch sphere, realizing a universal one-qubit gate. In addition, we have considered the effects of symmetries and disorder and have illustrated that these affects can be "gauged" away through calibrating the junction. Finally, we have discussed potential applications of the novel quantum point junction as the basic unit to imagine novel devices with applications in quantum computing and sensing. We hope that our approach will inspire new paths in exploring complex quantum systems.

VI. METHODS

a. Model Hamiltonian. We consider an adaptation of a simple four-band tight-binding model proposed by Bernevig et al.[49,50] to describe systems exhibiting a topological phase transition mediated by a single band inversion at Γ. The simplicity of the model makes detailed calculations practical even for large systems. The model is written in terms of two spinful orbitals per lattice site and takes the form

$$\begin{aligned} H_0 = m\sum_{\ell} c^\dagger_\ell \tau^z c_\ell + \frac{t}{2}{\sum_{\ell\ell'}}' c^\dagger_\ell \tau^z c_{\ell'} \\ + \frac{-i\lambda}{2}{\sum_{\ell\ell'}}' c^\dagger_\ell \tau^x \hat{\mathbf{n}}_{\ell\ell'}\cdot\boldsymbol{\sigma} c_{\ell'} + m_{\mathrm{Z}}\sum_{\ell}(-)^{\ell_z} c^\dagger_\ell \sigma^z c_\ell \ . \end{aligned} \tag{8}$$

Here ℓ labels a lattice site $\mathbf{R}_\ell = (\ell_x, \ell_y, \ell_z)$ on the unit cubic lattice, ${\sum}'_{\ell\ell'}$ indicates a sum over nearest neighbor sites, and $\hat{\mathbf{n}}_{\ell\ell'}$ is the nearest neighbor unit vector. We have adopted an implied sum notation for the orbital and spin degrees of freedom, e.g., $c^\dagger_\ell \tau^\mu \sigma^\nu c_{\ell'} = \sum_{ij,st} c^\dagger_{\ell is}\tau^\mu_{ij}\sigma^\nu_{st} c_{\ell' jt}$, where τ and σ are Pauli matrices for orbital and spin degrees of freedom respectively, and $c^\dagger_{\ell is}$ creates an electron on site ℓ in orbital i with spin s.

The first three terms in Eq. (8) correspond to the model of Bernevig et al.[49,50] for a strong topological insulator, often written in k-space as $H_{\mathrm{STI}}(\mathbf{k}) = m\tau^z + \sum_{i=x,y,z} t\cos(k_i)\tau^z + \lambda\sin(k_i)\tau^x\sigma^i$. In the last term in Eq. (8), m_{Z} is the strength of the staggered Zeeman field corresponding to A-type (layered) AFM order, doubling the unit cell and converting the model to represent an AFM topological insulator. Time reversal itself is now broken, but time reversal followed by a unit translation along $\hat{\mathbf{z}}$ is a good symmetry. For our choice of parameters,[40] the model is in the topological phase, with a formal magnetoelectric coupling of $(\theta/2\pi)(e^2/h)$ with axion coupling $\theta = \pi$. As a result, $\hat{\mathbf{z}}$-normal surfaces are naturally gapped and carry an anomalous Hall conductivity of $\pm e^2/2h$.

b. Wave-packet construction. We construct the initial WPs in the space of momentum $k_\parallel$ along the direction of propagation. We calculate the surface band structure for a supercell Hamiltonian H_{dw} or H_{st} containing a domain wall or step, whose presence results in mid-gap bands localized on the conducting channels in the otherwise gapped surface, as shown in Fig. 1**c**, **d** respectively. Note that technically each slab contains two domain walls and two steps. In the domain wall case the configuration as a whole is invariant under time reversal times inversion, so the bands shown are Kramers degenerate.

Next we construct the WP by making a quantum superposition of channel-localized solutions according to a $k_\parallel$-space envelope function that we take to be a Gaussian. This results in a WP that is localized in all three real space dimensions. This is then used as the initial wave function $\Psi(0)$ of the time-evolution problem for the much larger system that includes the QPJ and is described by the Hamiltonian H_{QPJ}. We have defined H_{QPJ} as the model Hamiltonian H_0 in the presence of an antiferromagnetic domain wall and a single-height step that intersect in the center of the surface. A more detailed description of the WP construction can be found in the Supplemental Information.

c. Wave-packet dynamics. To avoid finite-size effects, we require the system size L to be much larger than the extent of the WPs along the channel. When both a domain wall and step are present, momentum is no longer a good quantum number in any direction, so we compute the time evolution entirely in real space. This is done using Chebyshev series expansion methods[51] applied to the time-evolution operator e^{-iHt}. We use slabs of size 160×160 in-plane and 16 cells thick, enough to minimize finite-size effects, and adopt a Chebyshev expansion order of $N_C = 2^{11}$ so that we can time evolve the state accurately over the needed time intervals.

d. STM tip modeling. To model the effects of the magnetic and electrostatic STM tips we extend the QPJ Hamiltonian (H_{QPJ}) with two spatially dependent terms

$$\tilde{H}_{\rm QPJ} = H_{\rm QPJ} + V_{\rm Z} \sum_{\ell \in \Omega_{\rm Z}} c_\ell^\dagger \sigma^z c_\ell + V_{\rm G} \sum_{\ell \in \Omega_{\rm G}} c_\ell^\dagger c_\ell \,, \quad (9)$$

where the second term modifies the Zeeman interaction in a region $\Omega_{\rm Z}$ and the third term shifts the energy of all orbitals and spins uniformly inside a region $\Omega_{\rm G}$.

For a positive $V_{\rm Z}$ in Eq. (9), we choose the region $\Omega_{\rm Z}$ such that it restricts the sum to surface orbitals that lie within a radius r of the tip, and that already experience a negative Zeeman field from the bulk Hamiltonian of Eq. (8). Thus, $V_{\rm Z} = m_{\rm Z}$ is just enough to remove the Zeeman field from these sites, and $V_{\rm Z} = 2m_{\rm Z}$ makes the surface-layer Zeeman field equal on both sides of the domain wall or step, as in Fig. 4**a**. We can then tune between these extremes by taking $V_{\rm Z} \in [0, 2m_{\rm Z}]$, thus modeling cases in which the magnetic tip has only partially reversed the surface field. Similarly, for $V_{\rm Z} < 0$, $\Omega_{\rm Z}$ is chosen such that the second term in Eq. (9) is restricted to surface orbitals experiencing a positive Zeeman field in the bulk Hamiltonian.

The region of influence of the electrostatic tip, $\Omega_{\rm G}$ in Eq. (9), is defined to be a rectangle centered at (x_0, y_0) relative to the QPJ and one unit cell deep, as shown by the grey shading in Fig. 4**d**. A WP propagating for a distance ℓ along any domain-wall or step channel lying inside the quantum well defined by $\Omega_{\rm G}$ acquires an additional phase proportional to $\ell \Delta k$, where Δk is the shift of the Fermi wavevector of the channel. In the approximation of linear dispersion, we have $\Delta k = V_{\rm G}/\hbar v_F$, where $V_{\rm G}$ corresponds to a local gate voltage and v_F is the Fermi velocity (equal to $v_{\rm dw}$ and $v_{\rm st}$ for domain-wall and step channels respectively). Thus, the off-centering of $\Omega_{\rm G}$ defined by (x_0, y_0) allows us to control the travel distances ℓ along each of the four "legs" near the junction, introducing extra phases that are given by

$$\alpha = -\Delta k_{\rm dw} y_0, \;\; \gamma = -\Delta k_{\rm st} x_0 \quad (10)$$

in Eq. (7).

ACKNOWLEDGMENTS

This work is supported by NSF CAREER Grant No. DMR-1941569 (J.H.P.) and NSF Grant DMR-1954856 (N.V. and D.V.). The authors acknowledge the Beowulf cluster at the Department of Physics and Astronomy of Rutgers University, and the Office of Advanced Research Computing (OARC) at Rutgers, The State University of New Jersey (http://oarc.rutgers.edu), for providing access to the Amarel cluster and associated research computing resources that have contributed to the results reported here.

AUTHOR CONTRIBUTIONS

N.V. and D.V. conceived the project. N.V., J.H.W., J.H.P. set up the wave packet simulations that were performed by N.V.; All authors contributed to the theoretical analysis and the writing of the manuscript.

COMPETING INTERESTS

The authors declare no competing interests.

* nvarnava@physics.rutgers.edu

1 M. Z. Hasan and C. L. Kane, "Colloquium: Topological insulators," Rev. Mod. Phys. **82**, 3045–3067 (2010).

2 Xiao-Liang Qi and Shou-Cheng Zhang, "Topological insulators and superconductors," Rev. Mod. Phys. **83**, 1057–1110 (2011).

3 Chao-Xing Liu, Shou-Cheng Zhang, and Xiao-Liang Qi, "The quantum anomalous hall effect: Theory and experiment," Annual Review of Condensed Matter Physics **7**, 301–321 (2016).

4 Cui-Zu Chang, Jinsong Zhang, Xiao Feng, Jie Shen, Zuocheng Zhang, Minghua Guo, Kang Li, Yunbo Ou, Pang Wei, Li-Li Wang, Zhong-Qing Ji, Yang Feng, Shuaihua Ji, Xi Chen, Jinfeng Jia, Xi Dai, Zhong Fang, Shou-Cheng Zhang, Ke He, Yayu Wang, Li Lu, Xu-Cun Ma, and Qi-Kun Xue, "Experimental observation of the quantum anomalous hall effect in a magnetic topological insulator," Science **340**, 167–170 (2013).

5 Inhee Lee, Chung Koo Kim, Jinho Lee, Simon J. L. Billinge, Ruidan Zhong, John A. Schneeloch, Tiansheng Liu, Tonica Valla, John M. Tranquada, Genda Gu, and J. C. Séamus Davis, "Imaging dirac-mass disorder from magnetic dopant atoms in the ferromagnetic topological insulator crx(bi0.1sb0.9)2-xte3," Proceedings of the National Academy of Sciences **112**, 1316–1321 (2015).

6 J. G. Checkelsky, R. Yoshimi, A. Tsukazaki, K. S. Takahashi, Y. Kozuka, J. Falson, M. Kawasaki, and Y. Tokura, "Trajectory of the anomalous hall effect towards the quantized state in a ferromagnetic topological insulator," Nature Physics **10**, 731–736 (2014).

7 A. J. Bestwick, E. J. Fox, Xufeng Kou, Lei Pan, Kang L. Wang, and D. Goldhaber-Gordon, "Precise quantization of the anomalous hall effect near zero magnetic field," Phys. Rev. Lett. **114**, 187201 (2015).

8 Cui-Zu Chang, Weiwei Zhao, Duk Y. Kim, Haijun Zhang, Badih A. Assaf, Don Heiman, Shou-Cheng Zhang, Chaoxing Liu, Moses H. W. Chan, and Jagadeesh S. Moodera, "High-precision realization of robust quantum anomalous hall state in a hard ferromagnetic topological insulator," Nature Materials **14**, 473–477 (2015).

9 Yoshinori Tokura, Kenji Yasuda, and Atsushi Tsukazaki, "Magnetic topological insulators," Nature Reviews Physics **1**, 126–143 (2019).

10 Aaron L. Sharpe, Eli J. Fox, Arthur W. Barnard, Joe Finney, Kenji Watanabe, Takashi Taniguchi, M. A. Kastner, and David Goldhaber-Gordon, "Emergent ferro-

magnetism near three-quarters filling in twisted bilayer graphene," Science **365**, 605–608 (2019).

[11] M. Serlin, C. L. Tschirhart, H. Polshyn, Y. Zhang, J. Zhu, K. Watanabe, T. Taniguchi, L. Balents, and A. F. Young, "Intrinsic quantized anomalous hall effect in a moiré heterostructure," Science **367**, 900–903 (2020).

[12] Yujun Deng, Yijun Yu, Meng Zhu Shi, Zhongxun Guo, Zihan Xu, Jing Wang, Xian Hui Chen, and Yuanbo Zhang, "Quantum anomalous hall effect in intrinsic magnetic topological insulator mnbi2te4," Science **367**, 895–900 (2020).

[13] Joshua P. Wakefield and Joseph G. Checkelsky, "Two paths to intrinsic quantization," Science **367**, 848–849 (2020).

[14] Yan Gong, Jingwen Guo, Jiaheng Li, Kejing Zhu, Menghan Liao, Xiaozhi Liu, Qinghua Zhang, Lin Gu, Lin Tang, Xiao Feng, Ding Zhang, Wei Li, Canli Song, Lili Wang, Pu Yu, Xi Chen, Yayu Wang, Hong Yao, Wenhui Duan, Yong Xu, Shou-Cheng Zhang, Xucun Ma, Qi-Kun Xue, and Ke He, "Experimental realization of an intrinsic magnetic topological insulator," Chinese Physics Letters **36**, 076801 (2019).

[15] Jiaheng Li, Yang Li, Shiqiao Du, Zun Wang, Bing-Lin Gu, Shou-Cheng Zhang, Ke He, Wenhui Duan, and Yong Xu, "Intrinsic magnetic topological insulators in van der waals layered mnbi2te4-family materials," Science Advances **5** (2019), 10.1126/sciadv.aaw5685.

[16] Bo Chen, Fucong Fei, Dongqin Zhang, Bo Zhang, Wanling Liu, Shuai Zhang, Pengdong Wang, Boyuan Wei, Yong Zhang, Zewen Zuo, Jingwen Guo, Qianqian Liu, Zilu Wang, Xuchuan Wu, Junyu Zong, Xuedong Xie, Wang Chen, Zhe Sun, Shancai Wang, Yi Zhang, Minhao Zhang, Xuefeng Wang, Fengqi Song, Haijun Zhang, Dawei Shen, and Baigeng Wang, "Intrinsic magnetic topological insulator phases in the sb doped mnbi2te4 bulks and thin flakes," Nature Communications **10**, 4469 (2019).

[17] Xiangang Wan, Ari M Turner, Ashvin Vishwanath, and Sergey Y Savrasov, "Topological semimetal and Fermi-arc surface states in the electronic structure of pyrochlore iridates," Phys. Rev. B **83**, 205101 (2011).

[18] Nicodemos Varnava and David Vanderbilt, "Surfaces of axion insulators," Phys. Rev. B **98**, 245117 (2018).

[19] Nicodemos Varnava, Ivo Souza, and David Vanderbilt, "Axion coupling in the hybrid wannier representation," Phys. Rev. B **101**, 155130 (2020).

[20] E. Khalaf, "Higher-order topological insulators and superconductors protected by inversion symmetry," Phys. Rev. B **97**, 205136 (2018).

[21] M. Ezawa, "Magnetic second-order topological insulators and semimetals," Phys. Rev. B **97**, 155305 (2018).

[22] F. Schindler, A. M. Cook, M. G. Vergniory, Z. Wang, S. S. P. Parkin, B. A. Bernevig, and T. Neupert, "Higher-order topological insulators," Sci. Adv. **4** (2018), 10.1126/sciadv.aat0346.

[23] X. L. Qi, T. L. Hughes, and S. C. Zhang, "Topological field theory of time-reversal invariant insulators," Phys. Rev. B **78**, 195424 (2008).

[24] Andrew M. Essin, Joel E. Moore, and David Vanderbilt, "Magnetoelectric polarizability and axion electrodynamics in crystalline insulators," Phys. Rev. Lett. **102**, 146805 (2009), see also Erratum: Phys. Rev. Lett. **103**, 259902(E) (2009).

[25] Roger S. K. Mong, Andrew M. Essin, and Joel E. Moore, "Antiferromagnetic topological insulators," Phys. Rev. B **81**, 245209 (2010).

[26] M. M. Otrokov, I. I. Klimovskikh, H. Bentmann, D. Estyunin, A. Zeugner, Z. S. Aliev, S. Gaß, A. U. B. Wolter, A. V. Koroleva, A. M. Shikin, M. Blanco-Rey, M. Hoffmann, I. P. Rusinov, A. Yu. Vyazovskaya, S. V. Eremeev, Yu. M. Koroteev, V. M. Kuznetsov, F. Freyse, J. Sánchez-Barriga, I. R. Amiraslanov, M. B. Babanly, N. T. Mamedov, N. A. Abdullayev, V. N. Zverev, A. Alfonsov, V. Kataev, B. Büchner, E. F. Schwier, S. Kumar, A. Kimura, L. Petaccia, G. Di Santo, R. C. Vidal, S. Schatz, K. Kißner, M. Ünzelmann, C. H. Min, Simon Moser, T. R. F. Peixoto, F. Reinert, A. Ernst, P. M. Echenique, A. Isaeva, and E. V. Chulkov, "Prediction and observation of an antiferromagnetic topological insulator," Nature **576**, 416–422 (2019).

[27] Chaowei Hu, Kyle N. Gordon, Pengfei Liu, Jinyu Liu, Xiaoqing Zhou, Peipei Hao, Dushyant Narayan, Eve Emmanouilidou, Hongyi Sun, Yuntian Liu, Harlan Brawer, Arthur P. Ramirez, Lei Ding, Huibo Cao, Qihang Liu, Dan Dessau, and Ni Ni, "A van der waals antiferromagnetic topological insulator with weak interlayer magnetic coupling," Nature Communications **11**, 97 (2020).

[28] Yuanfeng Xu, Zhida Song, Zhijun Wang, Hongming Weng, and Xi Dai, "Higher-order topology of the axion insulator euin$_2$as$_2$," Phys. Rev. Lett. **122**, 256402 (2019).

[29] Yuanfeng Xu, Luis Elcoro, Zhida Song, Benjamin J. Wieder, M. G. Vergniory, Nicolas Regnault, Yulin Chen, Claudia Felser, and B. Andrei Bernevig, "High-throughput calculations of antiferromagnetic topological materials from magnetic topological quantum chemistry," (2020), arXiv:2003.00012.

[30] Paul M. Sass, Jinwoong Kim, David Vanderbilt, Jiaqiang Yan, and Weida Wu, "Robust a-type order and spin-flop transition on the surface of the antiferromagnetic topological insulator mnbi$_2$te$_4$," Phys. Rev. Lett. **125**, 037201 (2020).

[31] G. Fève, A. Mahé, J.-M. Berroir, T. Kontos, B. Plaçais, D. C. Glattli, A. Cavanna, B. Etienne, and Y. Jin, "An on-demand coherent single-electron source," Science **316**, 1169–1172 (2007).

[32] J. Dubois, T. Jullien, F. Portier, P. Roche, A. Cavanna, Y. Jin, W. Wegscheider, P. Roulleau, and D. C. Glattli, "Minimal-excitation states for electron quantum optics using levitons," Nature **502**, 659–663 (2013).

[33] D. Ferraro, B. Roussel, C. Cabart, E. Thibierge, G. Fève, Ch. Grenier, and P. Degiovanni, "Real-time decoherence of landau and levitov quasiparticles in quantum hall edge channels," Phys. Rev. Lett. **113**, 166403 (2014).

[34] D. Christian Glattli and Preden S. Roulleau, "Levitons for electron quantum optics," physica status solidi (b) **254**, 1600650 (2017).

[35] Leonid S. Levitov, Hyunwoo Lee, and Gordey B. Lesovik, "Electron counting statistics and coherent states of electric current," Journal of Mathematical Physics **37**, 4845–4866 (1996).

[36] D. A. Ivanov, H. W. Lee, and L. S. Levitov, "Coherent states of alternating current," Phys. Rev. B **56**, 6839–6850 (1997).

[37] J. Keeling, I. Klich, and L. S. Levitov, "Minimal excitation states of electrons in one-dimensional wires," Phys. Rev. Lett. **97**, 116403 (2006).

[38] D A Wharam, T J Thornton, R Newbury, M Pepper, H Ahmed, J E F Frost, D G Hasko, D C Peacock, D A Ritchie, and G A C Jones, "One-dimensional transport

and the quantisation of the ballistic resistance," Journal of Physics C: Solid State Physics **21**, L209–L214 (1988).

[39] B. J. van Wees, H. van Houten, C. W. J. Beenakker, J. G. Williamson, L. P. Kouwenhoven, D. van der Marel, and C. T. Foxon, "Quantized conductance of point contacts in a two-dimensional electron gas," Phys. Rev. Lett. **60**, 848–850 (1988).

[40] "See supplementary information.".

[41] More generally, systems that involve many junctions and result in $N > 2$ output channels will transform under $S \in \mathrm{SU}(N)$. In such cases each junction acts as $S \in U(2) \subset \mathrm{SU}(N)$. In this work we are only concerned with systems with $N = 2$, so that each junction acts as an SU(2) matrix.

[42] G. Cybenko, "Reducing quantum computations to elementary unitary operations," Computing in Science Engineering **3**, 27–32 (2001).

[43] A Ramamoorthy, J P Bird, and J L Reno, "Using split-gate structures to explore the implementation of a coupled-electron-waveguide qubit scheme," Journal of Physics: Condensed Matter **19**, 276205 (2007).

[44] Michihisa Yamamoto, Shintaro Takada, Christopher Bäuerle, Kenta Watanabe, Andreas D. Wieck, and Seigo Tarucha, "Electrical control of a solid-state flying qubit," Nature Nanotechnology **7**, 247–251 (2012).

[45] Paolo Bordone, Laura Bellentani, and Andrea Bertoni, "Quantum computing with quantum-hall edge state interferometry," Semiconductor Science and Technology **34**, 103001 (2019).

[46] H. Hffner, C.F. Roos, and R. Blatt, "Quantum computing with trapped ions," Physics Reports **469**, 155 – 203 (2008).

[47] Jay M. Gambetta, Jerry M. Chow, and Matthias Steffen, "Building logical qubits in a superconducting quantum computing system," npj Quantum Information **3**, 2 (2017).

[48] Biao Lian, Xiao-Qi Sun, Abolhassan Vaezi, Xiao-Liang Qi, and Shou-Cheng Zhang, "Topological quantum computation based on chiral majorana fermions," Proceedings of the National Academy of Sciences **115**, 10938–10942 (2018).

[49] B. Andrei Bernevig, Taylor L. Hughes, and Shou-Cheng Zhang, "Quantum spin hall effect and topological phase transition in hgte quantum wells," Science **314**, 1757–1761 (2006).

[50] Taylor L. Hughes, Emil Prodan, and B. Andrei Bernevig, "Inversion-symmetric topological insulators," Phys. Rev. B **83**, 245132 (2011).

[51] Alexander Weiße, Gerhard Wellein, Andreas Alvermann, and Holger Fehske, "The kernel polynomial method," Rev. Mod. Phys. **78**, 275–306 (2006).